Fibers and Polymers 2017, Vol.18, No.2, 349-356
DOI 10.1007/s12221-017-6522-3

ISSN 1229-9197 (print version)
ISSN 1875-0052 (electronic version)

An Improved Shear Lag Model for Predicting Stress Distribution in Hybrid Fiber Reinforced Rubber Composites

Bin Zhang*, Xiaoming Yu, and Boqin Gu[1]

School of Mechanical Engineering, Changshu Institute of Technology, Changshu 215500, China
[1]*College of Mechanical and Power Engineering, Nanjing Tech University, Nanjing 211816, China*
(Received May 11, 2016; Revised December 19, 2016; Accepted December 23, 2016)

Abstract: An improved micromechanical shear lag model, which considers the interphase and bonded fiber end, is developed to investigate the load-carrying characteristics and stress profiles in hybrid aramid/sepiolite fiber reinforced rubber composites. The properties of the equivalent matrix, which is combination of sepiolite fiber and rubber matrix, are determined by Mori-Tanaka method. The axial and shear stresses at the fiber end are resolved by the imaginary fiber technique. The results obtained from the improved model show the tensile stress has a maximal at the real fiber center and the interfacial shear stress has a maximal at the end of the real fiber. Comparing with the results from Tsai's model, the improved model has a better agreement with the numerical simualtion results. The effects of the imaginary fiber length on the stress transfer are analyzed and the results show that the effects can be ignored when the imaginary fiber length is greater than twice of the fiber radius. The effects of interphase modulus and thickness on the maximal axial and shear stresses are discussed. The results show that the interphase modulus and thickness of about 106.3 MPa and 0.2 μm are optimal to prevent interfacial debonding and improve the strength of hybrid fiber reinforced rubber composites.

Keywords: Hybrid fiber, Rubber composites, Interphase, Stress transfer, Imaginary fiber technique

Introduction

Fiber reinforced composites are widely used in petroleum, chemical, textile, electrical and mechanical industry, and their good applicability have been confirmed by engineering practices over recent years [1-3]. Hybrid fiber reinforced rubber composites (HFRR) are usually constituted of reinforcing fibers, compatibilization fibers, elastic binding materials, and chemical additives. Fibers or particles embedded in a rubber matrix can effectively improve the comprehensive performances such as strength intensity, fatigue resistance and corrosion resistance, etc. Elastic binding material binds reinforcing fibers, compatibilization fibers and chemical additives together, which makes up elastic network structure. Natural rubber (NR), nitrile rubber (NBR) and styrene-butadiene rubber (SBR), etc., can all be used as the elastic binding materials of HFRR among which nitrile rubber are preferably selected in consideration of product performances and cost [4].

As the bridge transmitting load between fiber and matrix material, interphase plays a dominant role in the performance of fiber reinforced composites [5-7]. It resides in a region between the original constituents of composites with a size ranging from several to hundreds of nanometers and is frequently modified by the use of coupling agents and sizings [8-10]. One difficulty encountered when modeling the interphase is the characterization of the dimensions and physical properties of the interphase. Currently the related parameters are mainly determined by experimental work. By using tapping mode phase imaging and nanoindentation tests based on the atomic force microscope, Gao *et al.* studied the sized fiber surface topography variation in the interphase of E-glass fiber-reinforced matrix composites. The interphase thickness is found to vary between 100 nm and 300 nm depending on the type of sizing and matrix materials. The modulus profiles indicated either a constant or a gradient in the modulus across the interphase due to the different interaction mechanisms of interphase [11]. Liu *et al.* used atomic force microscopy with force modulation mode to analyze the interphase of composites. The results show that the thickness of the transitional layer between carbon fiber and polyarylacetylene resin is more than 200 nm and the stiffness of the interphase is between the carbon fiber and PAA resin [12]. The thickness of interphase was estimated to be about 30 to 240 nm [13], and similar results were reported in an experimental study using scanning force microscopy [14]. However, other experimental findings suggest that the interphase within polymer matrix composites may be larger. The results obtained by secondary ion mass spectroscopy [15] and atomic force microscopy [16] indicate that the dimension of thickness magnitude is 1 μm for glass-fiber epoxy composites.

The shear lag model [17] is widely used to calculate deformational and elastic properties of fiber reinforced composites. The original model considers the load transfer from matrix to fiber by means of shear stress at the fiber-matrix interface, and several modifications have been made to account for the stress transfer and failure mechanisms in fiber-reinforced composites [18-21]. The accuracy of the model is largely dependent on the imposed boundary conditions at the fiber end. Generally, stress boundary conditions, based on arbitrary assumption, are predefined at

*Corresponding author: drzhbin@163.com

the fiber end to obtain the analytical solutions from the governing equations [22,23]. However, as Hsueh pointed out, these stresses cannot be predetermined, and therefore the boundary conditions are ambiguous. To solve this problem, a scheme was proposed by Hsueh [24] and Nair and Kim [25], where two imaginary fibers (made of matrix materials) were employed. This approach is the only one that gives the analytical solution to the stress distribution in matrix beyond the limit of the fiber end. However, a model incorporating the interphase is still to be developed.

In this work, an improved shear lag model is developed to investigate the load-carrying characteristics and stress profiles in HFRR made of reinforcing fiber (aramid fiber), elastic binding materials (NBR) and compatibilization fiber (sepiolite fiber). Imaginary fibers are added in the region from the fiber end to the surface of representative volume element (RVE) model. The properties of equivalent matrix are evaluated by the Mori-Tanaka method and the properties of the interphase are obtained by testing resorcinol formaldehyde latex (RFL) film. Then a finite element model is established to give numerical results to validate the accuracy of the improved shear lag model. Finally, the effects of interphase modulus and thickness on the maximal axial and shear stresses are discussed.

Analytical Model

Tsai's Model

Tsai *et al.* [26] developed a shear lag model which includes an interphase region between fiber and matrix material. Tsai's RVE model is shown in Figure 1, where the fiber end is subjected to a uniform tensile strain ε_0. The applied load is parallel to the fiber axis. The axial tensile stress $\sigma(r_f, x)$ and shear stress $\tau(r_f, x)$ in the cylindrical fiber are given by

$$\sigma(r_f,x) = E_f\varepsilon_0 + B\sinh(nx/r_f) + D\cosh(nx/r_f) \quad (1)$$

$$\tau(r_f,x) = -\frac{nr_f}{2}[D\sinh(nx/r_f) + B\cosh(nx/r_f)] \quad (2)$$

where

$$n = \sqrt{\frac{2G_iG_m}{E_f[G_m\ln(r_i/r_f) + G_i\ln(r_m/r_i)]}} \quad (3)$$

where E_f is the Young's modulus of fiber, G_i and G_m are the shear moduli of interphase and matrix, respectively. r_f, r_i and r_m are the radii of fiber, interphase and matrix, respectively. Constants B and D are dependent on the boundary conditions at the fiber end.

Applying the following boundary conditions

$$\sigma(r_f,l) = \sigma(r_f,-l) = 0 \quad (4)$$

The constants B and D can then be solved by equation (5).

$$\begin{cases} B = 0 \\ D = -E_f\varepsilon_0/\cosh(nl/r_f) \end{cases} \quad (5)$$

Hsueh's Model

Hsueh [24] added the imaginary fiber into the shear lag model. The tensile load is applied to the surface of RVE in the x direction. The fiber is bonded to the matrix at both the interface (i.e., at $r=r_f$) and the ends (i.e., at $x=\pm l$). The stress is transmitted from matrix to fiber through the interface and fiber end. Two parts of matrix that connect the fiber end to the loading surface (see the domain marked by dash lines in Figure 2) are treated as two imaginary fibers which have the same physical properties to matrix. Hence, the stress transfer problem depicted by Figure 2 can be solved using two shear lag models: one for $0 \le x \le l$ and the other for $l \le x \le L$. Although the stress at the fiber end is unknown, the two shear lag models are jointed at $x=l$ on the continuity condition, which, in turn, determines the stress at the fiber end.

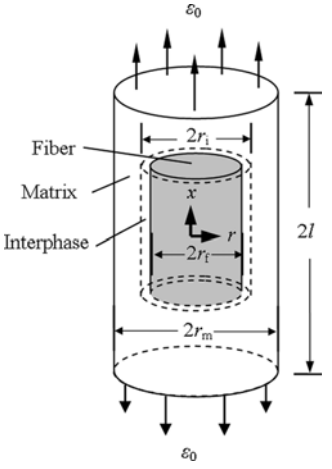

Figure 1. RVE model proposed by Tsai.

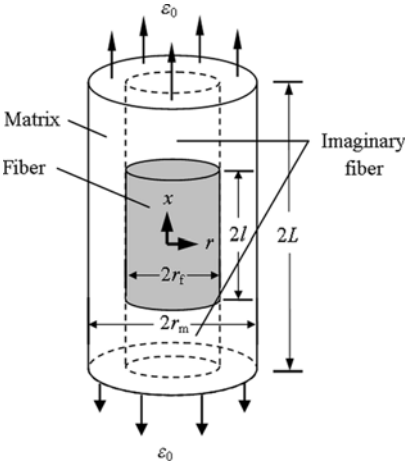

Figure 2. RVE model proposed by Hsueh.

Improved Model

When the fiber is embedded into the matrix with bonded fiber end, it requires a boundary condition to derive the stress at the fiber end. The Hsueh's model which has two imaginary fibers can give the stress at the fiber end, but the interphase existing in fiber reinforced composites is ignored. In order to investigate the stress transfer regularity in HFRR, a model which incorporates the imaginary fiber and interphase is developed, as shown in Figure 3. In the improved model, two imaginary fibers with length of $L-l$ and width of $r=r_f$ possess the same mechanical properties to that of the equivalent matrix material.

In the improved model, the axial tensile stress $\sigma_f(r_f, x)$ and interfacial shear stress $\tau_f(r_f, x)$ in the cylindrical fiber are given by equations (6) and (7), which have the similar form as equations (1) and (2).

$$\sigma_f(r_f,x) = E_f\varepsilon_0 + C_1\sinh(\alpha x/r_f) + C_2\cosh(\alpha x/r_f) \tag{6}$$

$$\tau_f(r_f,x) = -\frac{\alpha r_f}{2}[C_2\sinh(\alpha x/r_f) + C_1\cosh(\alpha x/r_f)] \tag{7}$$

where

$$\alpha = \sqrt{\frac{2G_iG_{em}}{E_f[G_{em}\ln(r_i/r_f) + G_i\ln(r_{em}/r_i)]}} \tag{8}$$

where G_{em} and r_{em} is the shear modulus and radius of the equivalent matrix. Constants C_1 and C_2 are dependent on the boundary conditions at the fiber end.

Considering the geometry similarity, equations (1) and (2) can also be used to describe the stress distribution along the imaginary fiber by replacing the Young's modulus of the fiber with that of the equivalent matrix. Thereby, the axial tensile stress $\sigma_{if}(r_f, x)$ and interfacial shear stress $\tau_{if}(r_f, x)$ in the imaginary fibers can be rewritten as

$$\sigma_{if}(r_f,x) = E_{em}\varepsilon_0 + C_3\sinh(\beta x/r_f) + C_4\cosh(\beta x/r_f) \tag{9}$$

$$\tau_{if}(r_f,x) = -\frac{\beta r_f}{2}[C_4\sinh(\beta x/r_f) + C_3\cosh(\beta x/r_f)] \tag{10}$$

$$\beta = \sqrt{\frac{1}{(1+\upsilon_{em})\ln(r_{em}/r_f)}} \tag{11}$$

where E_{em} and ν_{em} are the Young's modulus the Poisson's ratio of the equivalent matrix. C_3 and C_4 are dependent on the boundary conditions at the fiber end.

Applying the following boundary conditions (equation (12)) and using equations (6)-(11), the constants C_1, C_2, C_3 and C_4 can then be solved by equation (13).

$$\begin{cases} \sigma_f(r_f,l) = \sigma_{if}(r_f,l) \\ \tau_f(r_f,l) = \tau_{if}(r_f,l) \\ \tau_f(r_f,0) = 0 \\ \tau_{if}(r_f,L) = 0 \end{cases} \tag{12}$$

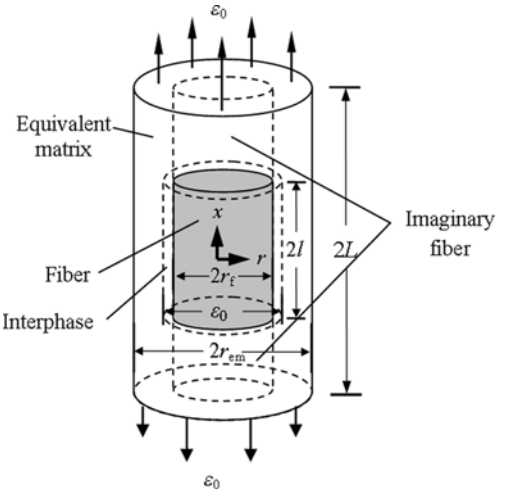

Figure 3. The improved micromechanical model of HFRR.

$$\begin{cases} C_1 = 0 \\ C_2 = [\beta C_4\sinh(\beta l/r_f) + \beta C_3\cosh(\beta l/r_f)]/[\alpha\sinh(\alpha l/r_f)] \\ C_3 = (E_f - E_m)\varepsilon_0/[\sinh(\beta l/r_f) - \coth(\beta L/r_f)\cosh(\beta l/r_f) \\ \quad + \frac{\beta}{\alpha}\left(\coth(\beta L/r_f)\sinh(\beta l/r_f)\coth(\alpha l/r_f) - \frac{\beta}{\alpha}\cosh(\beta l/r_f)\coth(\alpha l/r_f)\right)] \\ C_4 = -\coth(\beta L/r_f)C_3 \end{cases} \tag{13}$$

Properties of Equivalent Matrix and Interphase

Properties of Equivalent Matrix

Since the diameter of the sepiolite fiber (100 nm) is much less than that of the aramid fiber (15 μm) and the major reinforced phase in HFRR is the aramid fiber, the sepiolite fiber together with rubber can be replaced by an effective homogeneous matrix. The equivalent scheme by application of Mori-Tanaka method [27-30] is shown in Figure 4 and the method can be expressed by

$$[\boldsymbol{C}_{em}] = [\boldsymbol{C}_{rm}]([\boldsymbol{I}] + V_{sf}[\boldsymbol{A}])^{-1} \tag{14}$$

$$[\boldsymbol{A}] = \{[\boldsymbol{C}_{rm}] + ([\boldsymbol{C}_{sf}] - [\boldsymbol{C}_{rm}])[V_{sf}[\boldsymbol{I}] + (1-V_{sf})[\boldsymbol{S}_{ijkl}]]\}^{-1} \quad ([\boldsymbol{C}_m] - [\boldsymbol{C}_{sf}]) \tag{15}$$

where $[\boldsymbol{C}_{sf}]$, $[\boldsymbol{C}_{rm}]$ and $[\boldsymbol{C}_{em}]$ are the stiffness matrices of the sepiolite fiber, rubber and equivalent matrix, respectively. $[\boldsymbol{I}]$, $[\boldsymbol{S}_{ijkl}]$ and V_{sf} are the identity tensor, Eshelby tensor and volume fraction of the sepiolite fiber, respectively. For a spherical - like inclusion, $[\boldsymbol{S}_{ijkl}]$ is given in reference [30].

The mass ratio of the sepiolite fiber to rubber is assumed to 10:3 in HFRR. Since the densities of the sepiolite fiber and rubber are around 2.1 and 1.0 g/cm^3, respectively, the volume ratio is approximately 5:3. The modulus and Poisson's ratio of the sepiolite fiber are 86 GPa and 0.2, respectively [31,32]. The modulus of the rubber is about 2.5 MPa. On the basic of equations (14) and (15), the longitudinal Young's

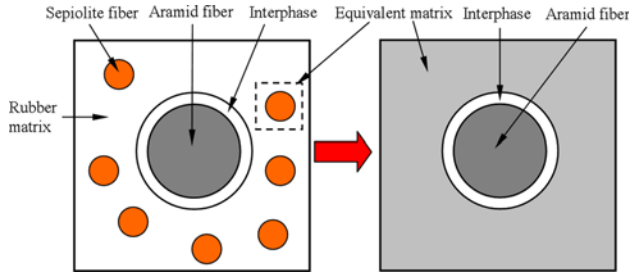

Figure 4. Equivalent principle by application of Mori-Tanaka method.

modulus and Poisson's ratio of the equivalent matrix is calculated to be 12.5 MPa and 0.45, respectively.

Properties of Interphase

The characterization of interphase modulus is difficult, and its result usually has large difference by different experimental methods. The test of the fiber surface treatment agent is an alternative method to characterize interphase properties. RFL-based dipping solution is common surface treatment agent for improving adhesion performance between the aramid fiber and rubber systems [33,34]. The RFL film specimen can be prepared by drying the RFL solution, and then the interphase properties can be obtained by measuring RFL film. Figure 5 is the RFL film specimen and its corresponding size is shown in Figure 6.

The properties of RFL film is determined by the dry weight ratio of resorcinol-formaldehyde (RF) to copolymer latex system (L), as shown in Table 1 [35,36]. The dry weight ratio of RF to L in this paper is between 0.1 and 0.25 and its corresponding tensile modulus is between 8.1 and 106.3 MPa. It can be also seen that the strength of RFL film is improved as dry weight ratio of RF to L increases.

Validation of the Improved Model

Finite Element Model

An axisymmetric finite element model of RVE is established based on the finite element analysis code ABAQUS, as shown in Figure 7. The model is given proportions such as L=0.13 mm and l=0.065 mm. The material parameters are

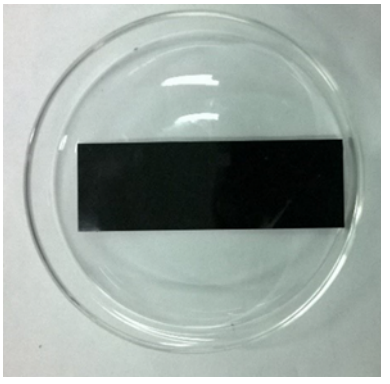

Figure 5. RFL film specimen.

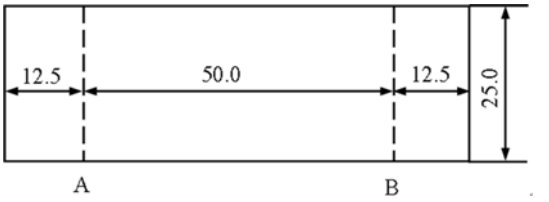

Figure 6. Specimen size of RFL film (unit mm).

Table 1. Mechanical properties of RFL films with different ratio of RF and L

RF/L	Tensile strength (MPa)	Tensile modulus (MPa)
10/100	4.5	8.1
14/100	7.6	17.0
16/100	8.0	23.9
18/100	9.1	41.2
20/100	12.1	65.4
25/100	15.1	106.3

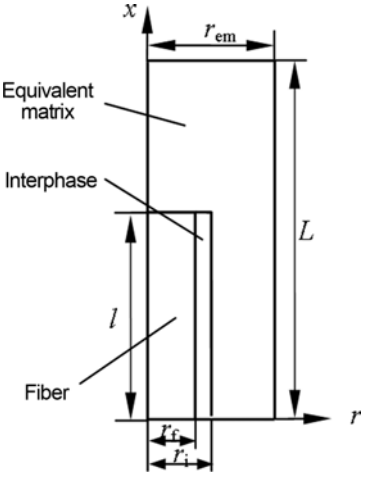

Figure 7. Axisymmetric finite element model of RVE.

Table 2. Material properties and dimension of RVE

Material parameter	Fiber	Equivalent matrix	Interphase
Young's modulus (MPa)	125000	12.5	41.2
Poisson's ratio	0.22	0.45	0.35
Diameter (mm)	0.013	0.026	0.0134

listed in Table 2. The 4-node bilinear axisymmetric quadrilateral with reduced integration and hourglass control element (CAX4R) is applied for the fiber, interphase and equivalent matrix. The mesh is graded so as to maximize the computational effort close to the fiber end, as shown in Figure 8, where the maximal stress concentration occurs. In radial direction, biased and gradually reduced elements are used for the fiber and matrix. A tensile load is applied on the surface of the RVE model. For the present finite element

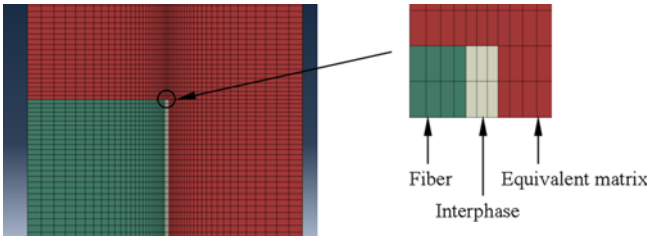

Figure 8. Grid of RVE.

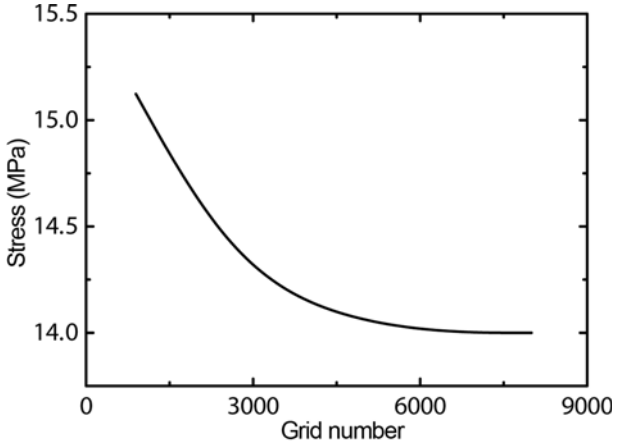

Figure 9. Independence analysis of grid.

model, the boundary conditions include:

$$\begin{cases} u_r = 0 \text{ at } r = 0 \\ u_x = 0 \text{ at } x = 0 \\ u_x = U \text{ at } x = L \\ u_r = a \text{ at } r = r_{em} \end{cases} \quad (16)$$

where u_r and u_x are the displacements in the r and x directions, respectively. U is the displacement at $x=L$ and a is a displacement varying with U. In the simulation, it is assumed that U is equal to 10 % of L, and the boundary of the model at $r=r_{em}$ is enforced to hold straight during deformation.

Grid independence analysis is conducted on the finite element model. Figure 9 shows that the magnitude of the tensile stress at the fiber end varies with the grid number. The result indicates that axial tensile stress approaches a stable value when the grid number is large than 6000. Therefore, the grid number of about 6000 is enough in the following finite element model.

Comparison of Results

In order to validate the accuracy of the improved model, the results among the finite element model, improved model and Tsai's model are compared, as shown in Table 3. The tensile stress at the fiber center and the shear stress at the fiber end are chosen as the analysis objects. The results show that the relative error between the improve model and finite element model is small (less than 5 %), and the relative error between the Tsai's model and finite element model is greater than 5 %. Therefore, the improved model is more appropriate to predict the stress distribution in HFRR.

Table 3. Comparison of calculation results

Stress	Finite element model	Tsai's model	Relative error (%)	Improved model	Relative error (%)
Tensile stress at the fiber center (MPa)	80.5	75.6	6.1	78.9	2.0
Shear stress at the fiber end (MPa)	6.8	6.2	8.8	6.5	4.4

Application of the Improved Model

The improved shear lag model is used to investigate the effects of the imaginary fiber length and interphase properties on the stress transfer regularity along the fiber axial direction. Unless otherwise indicated, the axial strain of the RVE is 10 % and material parameters are listed in Table 2 in the following analysis.

Stress Transfer Regularity

The stress distribution resulting from the improved model is investigated under the conditions of L/r_f=20, l/r_f=10, ε_0= 10 %. The tensile stress distribution along the fiber axial direction can be seen in Figure 10. The horizontal ordinate (x/r_f) denotes the distance from the fiber axial location to the fiber center (x=0). The dash dot line represents the boundary between the imaginary and real fiber. The tensile stress decreases as x/r_f increases in the real fiber and it has a maximal at the fiber center where the fiber fracture will occurs. In the imaginary fiber, the tensile stress continues to decrease as x/r_f increases and it approaches a stable value at the loading surface.

The interfacial shear stress along the fiber axial direction is shown in Figure 11. In the real fiber, the interfacial shear stress increases with the increment of x/r_f. The maximal interfacial shear stress occurs at the end of the real fiber where discontinuities of material properties exist. The interfacial shear stress will cause the interfacial debonding behavior. In the imaginary fiber, the interfacial shear stress decrease as x/r_f increases and its value is 0 at the loading surface.

Effect of Imaginary Fiber Length

The distributions of the axial tensile and interfacial shear stresses along the loading direction are shown in Figures 12 and 13, respectively, for different values of the imaginary fiber length ($L-l$). The results show that the tensile stress and interfacial shear stress have similar distribution rule. At the boundary between the imaginary and real fiber ($x=l$), the tensile stress has a finite value (Figure 12). This finite value decreases with an increase of the imaginary fiber length, and reaches an asymptotic value when the loading surface is

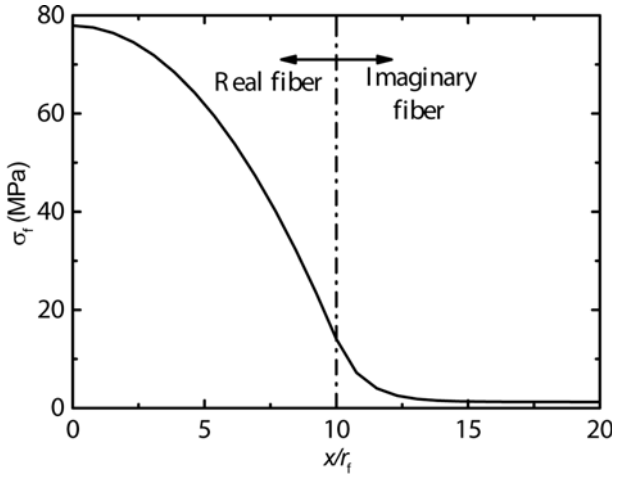

Figure 10. Tensile stress distribution along fiber axial direction.

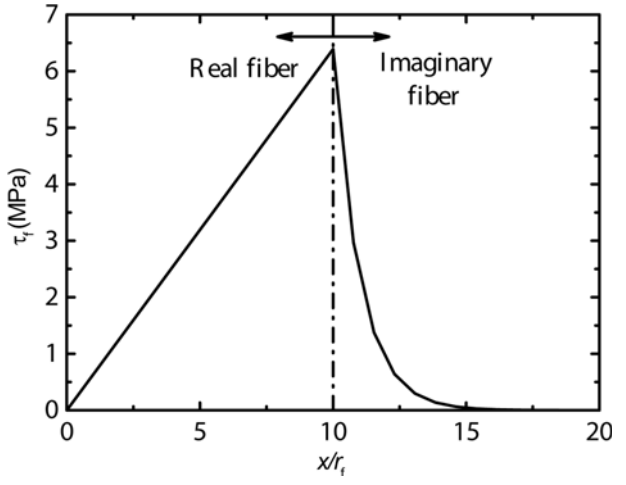

Figure 11. Interfacial shear stress distribution along fiber axial direction.

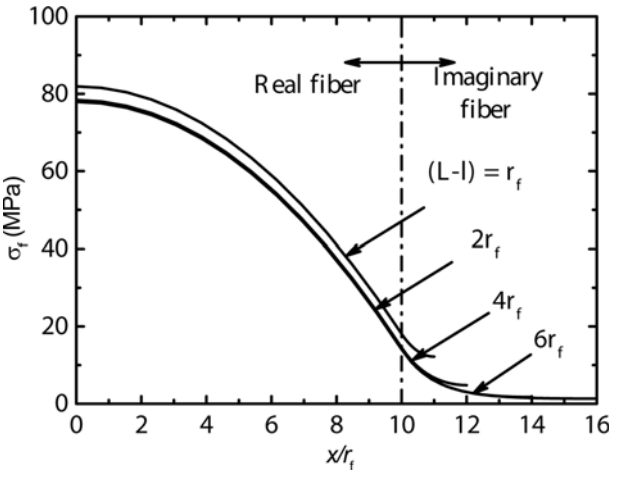

Figure 12. Tensile stress distribution for different values of imaginary fiber length.

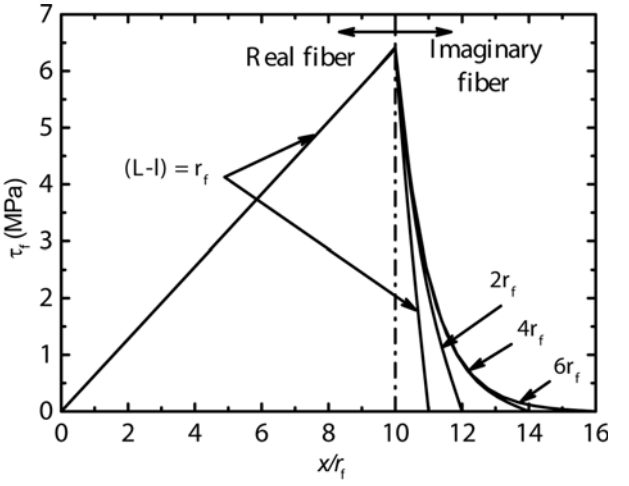

Figure 13. Interfacial shear stress distribution for different values of imaginary fiber length.

sufficiently remote from the fiber end. Figure 13 shows that there is little influence on the shear stress at the fiber end with different imaginary fiber lengths. The curves of interfacial shear stress distribution are overlapping in the real fiber and they are different in the imaginary fiber with different values of $L-l$.

It is noted that when the loading surface is sufficiently remote from the end of the real fiber, both σ_f and τ_f approach their asymptotic values at $x=l$. This condition can be satisfied when the distance between the loading surface and fiber end is larger than twice of the fiber radius, i.e. $(L-l) \geq 2r_f$. Hence, while analyzing the effects of the interphase properties on stress transfer in the next section, $(L-l)=2r_f$ is chosen and then the effect of the imaginary fiber length on stress transfer can then be ignored.

Effect of Interphase

From the above analysis results, the maximal tensile stress and interfacial shear stress occurs at the fiber center and fiber end, respectively. The fiber fracture and interfacial debonding will happen at those positions in fiber reinforced composites.

The effects of interphase on the tensile stress at the fiber center ($x=0$) and the interfacial shear stress at the fiber end ($x=l$) are shown in Figures 14 and 15. Figure 14 illustrates the influence of interphase modulus and thickness on the maximal tensile stress (σ_{max}). It can be seen that σ_{max} increases as the increase of interphase modulus. When the interphase modulus is less than 12.5 MPa, the maximal tensile stress increases significantly. That means the fiber bears a relative large axial load when the interphase modulus is large, as a result, the strength of HFRR will be enhanced. It can be also found that the tensile stress increases with the increasing interphase thickness when the interphase modulus is larger than 12.5 MPa, and it decreases with the increasing interphase thickness when the interphase modulus is smaller

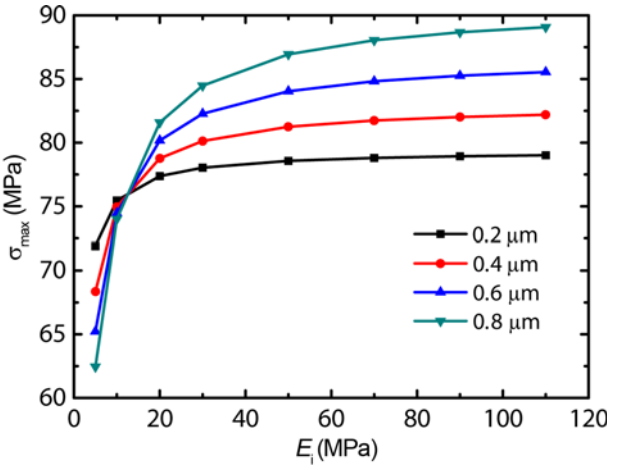

Figure 14. Variation of maximal tensile stress with interphase modulus and thickness.

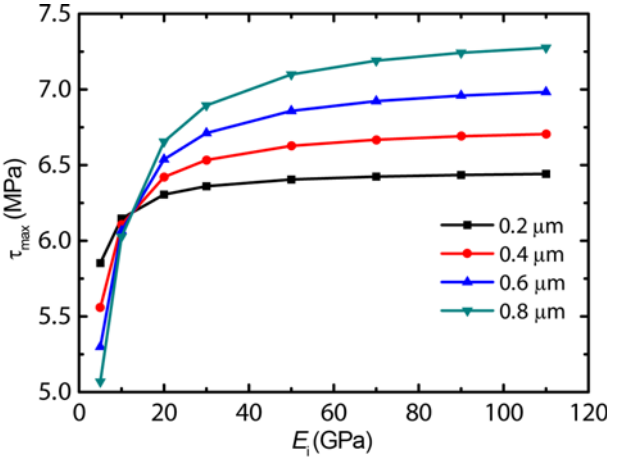

Figure 15. Variation of maximal interfacial shear stress with interphase modulus and thickness.

than 12.5 MPa. Therefore, it can be concluded that the stress transfer efficiency of HFRR can be enhanced by means of enhancing the interphase modulus and thickness.

The similar trend on the interfacial shear stress can be seen in Figure 15. The maximal interfacial shear stress (τ_{max}) increases as the interphase modulus increases. τ_{max} decreases with an increase in the interphase thickness when the interphase modulus is less than 12.5 MPa, and it increases with the increasing interphase thickness when the interphase modulus is larger than 12.5 MPa. The interfacial debonding is a main damage type in fiber reinforced rubber composites and a high interfacial shear stress will cause the damage of composites [8-10], so the low interfacial shear stress at the fiber end can prevent the generation of interfacial debonding effectively. The interphase properties are listed in Table 1. It can be seen that high tensile modulus corresponds to high interphase strength. Consequently, an interphase modulus of about of 106.3 MPa and an interphase thickness of about 0.2 μm are desired to prevent interfacial debonding and improve the strength of HFRR.

Conclusion

An improved shear lag model was developed to investigate the load-carrying characteristics and stress profiles in HFRR subjected to an axial load. The sepiolite fiber together with rubber matrix was replaced by an equivalent matrix and its property was obtained by Mori-Tanaka method.

The results of the improved model show that the maximal tensile stress occurs at the center of the real fiber where the fiber fracture will happen, and the maximal interfacial shear stress occurs at the end of the real fiber where the interfacial debonding will generate. It can be also obtained that the results of the improved model show a better agreement with the numerical simualtion results, comparing with the results from Tsai's model.

The effects of the imaginary fiber length, interphase modulus and thickness on the stress transfer efficiency were discussed. The effect of the imaginary fiber length on stress transfer can be ignored when it is larger than twice of the fiber radius. An interphase modulus of about 106.3 MPa and an interphase thickness of about 0.2 μm are desired to prevent interfacial debonding and improve the strength of HFRR.

Acknowledgement

This project is supported by National Natural Science Foundation of China (Grant No. 51375223) and by Scientific Research Foundation for Advanced Talents (XZ1517).

References

1. M. Jacob, S. Thomas, and K. T. Varughese, *Compos. Sci. Technol*., **64**, 955 (2004).
2. X. Yu, B. Gu, and B. Zhang, *Fiber. Polym*., **16**, 2258 (2015).
3. S. Li, Q. Lin, H. Zhu, C. Cui, H. Hou, T. Lv, and Y. Li, *Fiber. Polym*., **17**, 282 (2016).
4. B. Q. Gu, Y. Chen, and J. F. Zhou in "Advances in Composite Materials - Ecodesign and Analysis", 1st ed., pp.21-54, InTech, Rijeka, Croatia, 2011.
5. X. Wang, J. Zhang, Z. Wang, S. Zhou, and X. Sun, *Mater. Des*., **32**, 3486 (2011).
6. R. Haque, M. Saxena, S. C. Shit, and P. Asokan, *Fiber. Polym*., **16**, 146 (2015).
7. M. T. Zafar, S. N. Maiti, and A. K. Ghosh, *Fiber. Polym*., **17**, 266 (2016).
8. H. Zhang and W. Li, *J. Reinf. Plast. Compos*., **33**, 1520 (2014).
9. B. Xiao, Y. Yang, X. Wu, M. Liao, R. Nishida, and H. Hamada, *Fiber. Polym*., **16**, 1759 (2015).

10. L. X. Gong, L. L. Hu, J. Zang, Y. B. Pei, L. Zhao, and L. C. Tang, *Fiber*. *Polym*., **16**, 2056 (2015).
11. S. L. Gao and E. Mäder, *Compos. Pt. A-Appl. Sci. Manuf*., **33**, 559 (2002).
12. L. Liu, Y. J. Song, H. J. Fu, Z. X. Jiang, X. Z. Zhang, L. N. Wu, and Y. D. Huang, *Appl. Surf. Sci*., **254**, 5342 (2008).
13. Y. Termonia, *J. Mater. Sci*., **25**, 103 (1990).
14. M. Munz, H. Sturm, E. Schulz, and G. Hinrichsen, *Compos. Pt. A-Appl. Sci. Manuf*., **29**, 1251 (1998).
15. J. L. Thomason, *Composites*, **26**, 487 (1995).
16. K. Mai, E. Mäder, and M. Mühle, *Compos. Pt. A-Appl. Sci. Manuf*., **29**, 1111 (1998).
17. H. L. Cox, *Br. J. Appl. Phys*., **3**, 72 (1952).
18. C. Liu, X. Wang, and Y. Wang, *J. Reinf. Plast. Compos*., **33**, 1105 (2014).
19. K. T. Kashyap, P. G. Koppad, K. B. Puneeth, H. A. Ram, and H. M. Mallikarjuna, *Comput. Mater. Sci*., **50**, 2493 (2011).
20. L. Mishnaevsky and P. Brøndsted, *Comput. Mater. Sci*., **44**, 1351 (2009).
21. K. K. Ang and K. S. Ahmed, *Compos. Pt. B-Eng.,* **50**, 7 (2013).
22. V. C. Nardone and K. M. Prewo, *Scr. Metall. Mater*., **20**, 43 (1986).
23. T. W. Clyne, *Mater. Sci. Eng. A-Struct*., **122**, 183 (1989).
24. C. H. Hsueh, *J. Mater. Sci*., **30**, 219 (1995).
25. S. V. Nair and H. G. Kim, *J. Appl. Mech*., **59**, 176 (1992).
26. H. C. Tsai, A. M. Arocho, and L. W. Gause, *Mater. Sci. Eng. A-Struct*., **126**, 295 (1990).
27. N. K. Anifantis, *Compos. Sci. Technol*., **60**, 1241 (2000).
28. Y. Benveniste, *Mech. Mater*., **6**, 147 (1987).
29. P. Georgiopoulos and E. Kontou, *J. Reinf. Plast. Compos*., **33**, 942 (2014).
30. M. Taya and T. W. Chou, *Int. J. Solids Struct*., **17**, 553 (1981).
31. F. C. Basurto, D. García-López, N. Villarreal-Bastardo, J. C. Merino, and J. M Pastor, *Compos. Pt. B-Eng.,* **47**, 42 (2013).
32. G. Tartaglione, D. Tabuani, G. Camino, and M. Moisio, *Compos. Sci. Technol*., **68**, 451 (2008).
33. M. Shirazi, M. B. de Rooij, A. G. Talma, and J. W. M. Noordermeer, *J. Adhes. Sci. Technol*., **27**, 1886 (2013).
34. G. S. Shibulal and K. Naskar, *J. Polym. Res*., **18**, 2295 (2011).
35. M. Shen, J. Zhang, and Q. Chen, *J. Appl. Polym. Sci*., **113**, 3350 (2009).
36. B. Zhang, B. Gu, and X. Yu, *J. Appl. Polym. Sci*., **132**, 41672 (2015).